Spatial Equivalent Impedance Model Based Initial Position Detection for PMSM With High-Frequency Injection

Qiyao Li, Qiwei Wang, *Member, IEEE*, Gaolin Wang, *Senior Member, IEEE*, Fengxiang Wang, *Senior Member, IEEE*, Guoqiang Zhang, *Senior Member, IEEE*, and Dianguo Xu, *Fellow, IEEE*

***Abstract*—Accurate initial position detection is important for enhancing the start-up performance of permanent magnet synchronous motors (PMSMs). However, the conventional high-frequency (HF) injection methods make it difficult to estimate the accurate initial position in PMSMs with low saliency ratios and significant cogging harmonics. To address these issues, this article proposes a spatial equivalent impedance model based initial position detection method. First, a quasi-sinusoidal functional model containing the spatial equivalent impedance information is established, where the effect of cogging harmonics on initial position detection can be reduced. Moreover, the overall spatial equivalent impedance information is considered in the proposed method, which improves the estimation accuracy on low-saliency PMSMs. To suppress the fluctuation error of estimation results, a variable forgetting factor sliding discrete Fourier transform algorithm is presented. Furthermore, to enhance the universality of the proposed method, an adaptive HF amplitude selection method based on split-step HF injection is given. In the same process, the magnetic polarity detection is achieved simultaneously by HF current peak-value accumulation, where the process of dual-pulse injection can be eliminated. Finally, the proposed method is verified on a 2.2-kW interior PMSM (IPMSM) and a 7.5-kW surface PMSM (SPMSM).**

***Index Terms*—HF injection, initial position detection, magnetic polarity detection, permanent magnet synchronous motors (PMSMs), spatial equivalent impedance model (SEIM).**

I. Introduction

THE permanent magnet synchronous motors (PMSMs) are widely used in industrial drives due to their high efficiency, high reliability, and high power density [1], [2], [3]. The start-up of PMSMs needs the accurate initial position information to guarantee satisfying the load capacity with proper control current [4], [5]. Conventional rotor presetting methods inject dc currents before starting. However, the rotor is not allowed to rotate before start-up in some applications [6]. Therefore, it is necessary to research the rotor initial position detection methods. Currently, the initial position detection methods can be classified into two categories: pulse signal injection methods and high-frequency (HF) signal injection methods.

The pulse signal injection methods estimate the initial position by the inductance differences under different rotor positions. These methods inject the voltage pulses into the stator windings and compare the amplitude of the sampled currents to identify the minimum inductance of the motor, thereby detecting the rotor position [7]. To improve the detection accuracy, it is necessary to increase the density of the injected direction, which conversely extends the initial position detection time [8]. In [9], an iterative convergence based detection method was proposed, where the injected pulse signals gradually converged to the *d*-axis, improving the utilization rate of pulse voltage vectors. The pulse signal injection methods typically require injecting relatively large currents, which may result in significant noise and a nonzero average electromagnetic torque [10], [11].

The HF injection methods achieve the initial position detection by two steps, which contain the position estimation and magnetic polarity detection [12]. The position estimation methods can be further categorized into the HF rotating signal injection methods and the HF pulsating signal injection methods [13]. The HF rotating injection methods inject HF signals into the stationary reference frame, and the rotor position is observed through signal demodulations and observers [14]. In comparison, the HF pulsating injection methods inject HF signals into the estimated reference frame, and then the rotor position is detected by converging the estimated *d*-axis to the real *d*-axis [15]. For improving the estimation precision of the initial position, the negative effects in PMSM should be considered, such as the cross-coupling effect, inverter nonlinearities, stator resistance, and cogging harmonics. In [16], an accurate model of IPMSM was applied to eliminate the error caused by ignoring the stator resistance. In [17], a carrier injection method was proposed to reject the estimation error due to the stator resistance and time delays. As for the cross-coupling effect, the characteristics

Received 3 April 2025; revised 4 July 2025; accepted 8 August 2025. Date of publication 13 August 2025; date of current version 22 October 2025. This work was supported in part by the Research Fund for the National Natural Science Foundation of China under Grant 52307048, in part by the Delta Power Electronics Science and Education Development Program of Delta Group under Grant DREG2024008, in part by the Financial Assistance under Heilongjiang Postdoctoral Fund under Grant LBH-Z23022, and in part by the Heilongjiang Natural Science Foundation under Grant LH2024E047. Recommended for publication by Associate Editor J. Hur. *(Corresponding author: Qiwei Wang.)*

The authors are with the School of Electrical Engineering and Automation, Harbin Institute of Technology, Harbin 150001, China (e-mail: wqwhit@hit.edu.cn).

Color versions of one or more figures in this article are available at https://doi.org/10.1109/TPEL.2025.3598313.

Digital Object Identifier 10.1109/TPEL.2025.3598313

of the estimation error under different operation conditions were analyzed, along with the error compensation methods by the motor parameters identification or finite element analysis methods [18], [19]. In the aspect of inverter nonlinearity effects, the effects lead to distortion of the injected HF signal, which can be viewed as the disturbance voltage generators [20], [21]. The inverter nonlinearity effects could be compensated by the method in paper [22], which injected *d*-axis currents to obtain the inverter nonlinearity error voltages.

However, some other nonideal factors, such as the cogging harmonics introduced by the cogging effects, have not been taken into account. Cogging harmonics can cause the impedance harmonics of PMSMs [23], [24], [25]. In paper [24], an air-gap function with cogging harmonics was described, and the impedance expression with harmonics was derived. In paper [25], the harmonic functions were constructed to describe the *dq*-axis inductances with cogging harmonics. Moreover, the cogging harmonics can lead to the equivalent impedance harmonics, which are the disturbance in the initial position detection process. Furthermore, in low-saliency PMSMs, the difference of the *dq*-axis inductances is weaker (close to 0), and the cogging harmonics are relatively significant, which will increase the initial position estimation errors.

Moreover, to improve the estimation accuracy of PMSMs with different saliency ratios, the HF signal amplitude selection methods need to be investigated. In paper [26], the current amplitude was set to at least ten times the sampling standard deviation of the current sensors to achieve high-precision and high-reliability initial position detection. In paper [27], a minimum threshold of HF amplitude was given to decrease the sensitivity to noise of the proposed algorithm. In paper [28], a relationship between the quantization error of the analog-to-digital (AD) converter and the position estimation error was established, and then the boundary of the injected voltage was obtained. However, to enhance the universality of the proposed method in PMSMs with different saliency ratios, the adaptive HF amplitude selection method needs further research.

The HF injection methods require polarity identification after the position estimation process. The magnetic polarity detection based on dual-pulse voltage injection has been widely applied, which detected the magnetic polarity by comparing the currents in the positive and negative *d*-axes. These methods injected substantial pulse voltages to detect magnetic polarity, which might lead to the permanent magnet demagnetization and high noise [29]. Similar to the dual-pulse injection-based methods, the peak-value accumulation-based methods were proposed in paper [15], where the magnetic polarity can be obtained by comparing the current amplitude in the positive and negative *d*-axes. Other methods detected the second harmonic of the current to obtain magnetic polarity, whose signal-to-noise ratio (SNR) is low, and the magnetic polarity detection might fail [30]. However, these methods are achieved only when the rotor position has been observed.

This article proposes a spatial equivalent impedance model (SEIM) based initial position detection method. First, a quasi-sinusoidal functional model with the overall spatial equivalent impedances is established, where the rotor position is the phase of the fundamental component and the cogging harmonics are equivalent to the harmonic components. With the injection of a rotating HF voltage, the phase of the fundamental component of the current amplitude can be extracted by a variable forgetting factor sliding discrete Fourier transform (VFF-SDFT). It will reduce estimation errors caused by the cogging harmonics by decoupling the fundamental component of the current amplitude from the cogging harmonics. Then, an adaptive HF amplitude selection method based on split-step injection (SSHI) is proposed. This method establishes a relationship between the current amplitude and the saliency ratio, reconstructing the amplitude by injecting signals at different positions and achieving adaptive selection of the voltage amplitude. Simultaneously, the magnetic polarity is detected by comparing the peak value of the HF currents. The proposed method offers the following contributions.

1) The SEIM based method extracts the overall spatial equivalent impedance information and calculates the initial position by the fundamental phase of the spatial equivalent impedances. The proposed method decreases the initial position estimation errors introduced by the cogging harmonic, improving the estimation precision especially for SPMSM.
2) The SSHI based method achieves the adaptive HF amplitude selection for different saliency-ratio PMSMs and magnetic polarity detection simultaneously. The relatively small HF current is injected by the adaptive HF amplitude selection and the estimation precision can be ensured. In the same process, the magnetic polarity is detected by judging the magnetic polar regions, which can be obtained by the peak-value accumulation method. The dual-pulse voltage injection is avoided.

II. Spatial Equivalent Impedance Model of PMSMs

A. Spatial Equivalent Impedance Model of PMSMs

The initial position detection is implemented based on the PMSM model. The mathematical model in the *dq*-axes can be expressed as follows:

$$\begin{bmatrix} u_{\mathrm{d}} \\ u_{\mathrm{q}} \end{bmatrix} = \begin{bmatrix} R_{\mathrm{s}} + pL_{\mathrm{d}} & -\omega_{\mathrm{e}} L_{\mathrm{q}} \\ \omega_{\mathrm{e}} L_{\mathrm{d}} & R_{\mathrm{s}} + pL_{\mathrm{q}} \end{bmatrix} \begin{bmatrix} i_{\mathrm{d}} \\ i_{\mathrm{q}} \end{bmatrix} + \begin{bmatrix} 0 \\ \omega_{\mathrm{e}} \psi_{\mathrm{f}} \end{bmatrix} \tag{1}$$

where $\mathrm{u_d}$, u_{q}, i_{d}, and i_{q} are the voltages and currents in the *dq*-axes, respectively, R_{s} is the stator resistance, L_{d} and L_{q} are the inductances in the *dq*-axes, respectively, ψ_{f} is the permanent magnet linkage, and p is the derivative operator.

The position relationship is established in Fig. 1. To analyze the relationship between equivalent impedance and rotor position, an mn-frame is established, where the angle between the *m*-axis and the α-axis is θ_{m}. The equivalent impedance in the *m*-axis is defined as the special equivalent impedance. The rotor position is represented by θ_{e}.

When $\omega_{\mathrm{e}} = 0$, the motor equations in the *mn*-axes can be expressed as follows by coordinate transformation:

$$\begin{bmatrix} u_{\mathrm{m}} \\ u_{\mathrm{n}} \end{bmatrix} = R_{\mathrm{s}} \begin{bmatrix} i_{\mathrm{m}} \\ i_{\mathrm{n}} \end{bmatrix} + \begin{bmatrix} L_{\mathrm{mm}} & L_{\mathrm{mn}} \\ L_{\mathrm{mn}} & L_{\mathrm{nn}} \end{bmatrix} \begin{bmatrix} \mathrm{p}i_{\mathrm{m}} \\ \mathrm{p}i_{\mathrm{n}} \end{bmatrix} \tag{2}$$

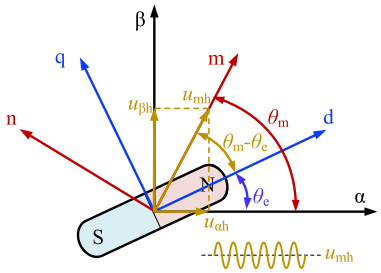

Fig. 1. Reference frames of PMSM for spatial equivalent impedance model.

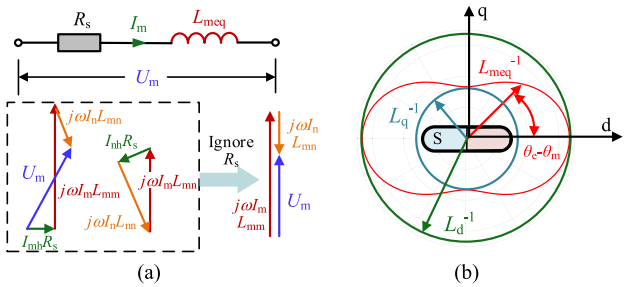

Fig. 2. Diagram of the spatial equivalent impedance model in the *mn*-axes. (a) Diagram of vector relationship in the *mn*-axes. (b) Polar diagram of L_{meq}.

where L_{mm}, L_{nn}, and L_{mn} can be expressed as follows:

$$\begin{cases} L_{mm} = L_\Sigma - L_\Delta \cos(2\theta_e - 2\theta_m) \\ L_{nn} = L_\Sigma + L_\Delta \cos(2\theta_e - 2\theta_m) \\ L_{mn} = L_\Delta \sin(2\theta_e - 2\theta_m) \end{cases} \tag{3}$$

where $L_\Delta = (L_q - L_d)/2$, $L_\Sigma = (L_q + L_d)/2$.

On this basis, the spatial equivalent impedance Z_m is

$$Z_m(\theta_m, \theta_e) = R_s + j\omega_h L_{meq}(\theta_m, \theta_e) \tag{4}$$

where ω_h is the frequency of the HF signal and L_{meq} is the spatial equivalent inductance.

If the resistance R_s can be neglected, the voltage equations in the *mn*-axes can be viewed as a series of self-inductances and mutual inductances. When the HF voltages are only injected into the *m*-axis, the voltage equations can be rewritten as follows:

$$\begin{bmatrix} u_m \\ 0 \end{bmatrix} = \begin{bmatrix} L_{mm} & L_{mn} \\ L_{mn} & L_{nn} \end{bmatrix} \begin{bmatrix} pi_m \\ pi_n \end{bmatrix}. \tag{5}$$

According to the impendence relationship of PMSM, let L_{meq} be equal to u_m/pi_m. Therefore, the spatial equivalent inductance L_{meq} can be expressed as follows:

$$L_{meq} = L_{mm} - \frac{L_{mn}^2}{L_{nn}} = \left[\frac{L_\Sigma}{L_d L_q} + \frac{L_\Delta \cos(2\theta_e - 2\theta_m)}{L_d L_q} \right]^{-1}. \tag{6}$$

In (3), the phase of L_{meq} is related to θ_m and θ_e. Therefore, the phase of the spatial equivalent impedance Z_m is also dependent on the rotor position.

In the above spatial equivalent impedance model, the relationship between the HF voltage and current signals is illustrated in Fig. 2(a). When ω_h is high, the R_s $[i_m, i_n]^T$ can be neglected, making the voltage vector model only related to the equivalent inductance L_{meq}. Therefore, U_m is only determined by the voltage drop on the L_{meq}. Thus, the voltage vectors transform into a straight-line relationship as shown in Fig. 2(a). Similarly, Z_m only depends on L_{meq}. The polar diagram of L_{meq}^{-1} is shown in Fig. 2(b), whose value depends on θ_e. In addition, according to (6), the phase of L_{meq} contains the information of rotor position.

In summary, θ_e is relevant to the phase of Z_m, which can be calculated by the HF injection-based methods. Furthermore, since the rotor position estimation is achieved by the saliency of the spatial equivalent impedance, the initial position of SPMSM, which exhibits weak saliency or saturated saliency, can also be estimated by the proposed method.

B. Influence of Cogging Harmonics and Saliency Ratio

In actual applications, the cogging effect can introduce harmonics into the spatial equivalent impedance Z_m and equivalent inductance L_{meq} [24], [25]. These harmonics lead to a shift in the salience position, resulting in initial position estimation errors. The magnetic circuit inductance can be expressed as follows:

$$L_x = \mu_x N_c A_x / l_x \tag{7}$$

where L_x is the equivalent inductance in any direction, μ_x is the relative magnetic conductivity, N_c is the winding factor, A_x is the equivalent square, and l_x is the equivalent length of the magnetic circuit.

The magnetic circuit lengths of the *dq*-axes are different, so L_x varies with position. Besides, the magnetic circuit lengths are different at the positions of the slots and the teeth. Therefore, the harmonics exist in the L_x. The spatial equivalent inductances L_{meq_all} considering the harmonics can be expressed as follows:

$$\begin{cases} L_{meq\_all}^{-1} = L_{meq}^{-1} + L_{meq\_har}^{-1} \\ L_{meq\_har}^{-1} = L_{meq\_slot}^{-1} \cos(k_h \theta_e + \varphi_{har}) \end{cases} \tag{8}$$

where k_h is the frequency of the impedance harmonics, φ_{har} is the phase of the harmonic components. The spatial equivalent inductance curves with and without harmonics are illustrated in Fig. 3. L_{meq} represents the ideal inductance curve. L_{meq_all} is the actual inductance curve with impedance harmonics, expressed by (8). When the cogging harmonics exist, they may lead to abrupt changes in the impedance values at specific positions, thereby causing a shift in the salience position. In Fig. 3, point *a* is the rotor position, while point *b* shows the possible convergence position around the salience position during the process of the HF based initial position detection. Due to the influence of the impedance harmonics, the estimated rotor position by the HF method may converge to *b*, which will result in the estimation error. Since the harmonic components of the L_{meq_all} are non-negligible in PMSMs with low saliency ratios, this error is more obvious. Ignoring the harmonic components of the L_{meq_all} may lead to a significant error in the estimation results.

It is important to note that the fundamental component of L_{meq} in Fig. 3 only depends on the rotor position, which is immune to the harmonics caused by the cogging effect. Therefore, the rotor position can be calculated by the fundamental component of L_{meq_all}, decreasing the influence of cogging harmonics and achieving high-precision position estimation.

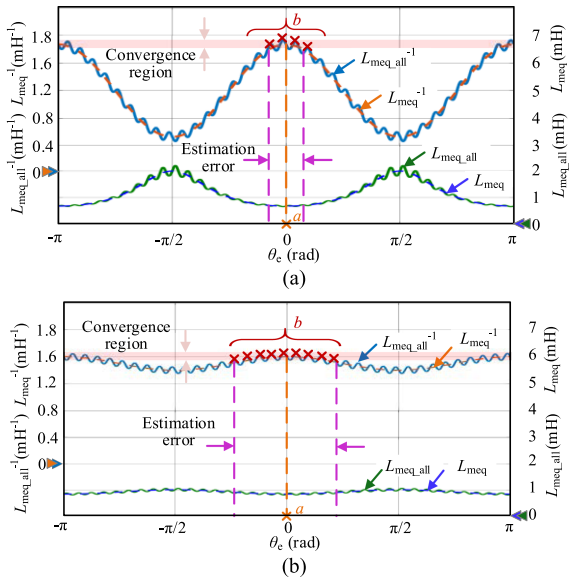

Fig. 3. Diagram of spatial equivalent inductance curves with and without harmonics in different L_q/L_d PMSMs. (a) $L_q/L_d = 3$. (b) $L_q/L_d = 1.2$.

III. SEIM Based Initial Position Detection Method

The diagram of the proposed initial position detection method is shown in Fig. 4. The proposed method is applied in two steps. The first step is the SSHI based HF amplitude adaptive selection method and peak-value accumulation based magnetic polarity detection method. The second step is the SEIM based initial position estimation method. Following the second step, the estimation result is compensated by the magnetic polarity detection result obtained in the first step. In the position estimation process, the band bass filter is applied to extract the HF signals and avoid the influence of the switching frequency. DFT is used to obtain the amplitudes and phases of the HF signals. The proposed VFF-SDFT method aims to calculate the phases of currents and estimate the rotor position. In the magnetic polarity detection process, the DFT is employed to obtain the HF amplitudes in the r_1-, r_2-, and r_3-axes, which can be used for the adaptive selection of amplitude and the magnetic region detection.

A. SEIM Based Initial Position Estimation

The proposed method injects a rotational HF voltage vector u_{mh} to excite the current response in the m-axis. The amplitude of the HF current response I_{mh} is computed by the DFT method. Subsequently, the rotor position estimation is converted to the phase calculation of the fundamental component of I_{mh}.

The m-axis is the injection axis, whose rotational frequency is ω_m. The HF voltage in the mn-axes can be expressed as follows:

$$\begin{bmatrix} u_{mh} \\ u_{nh} \end{bmatrix} = \begin{bmatrix} U_{mh} \sin(\omega_h t + \varphi_u) \\ 0 \end{bmatrix} \tag{9}$$

where U_{mh}, ω_h, and φ_u are the amplitude, frequency, and phase of the injected HF signal, respectively. The subscript h represents the HF components.

When the m-axis rotates at a frequency of ω_m, the voltage equations can be written as follows:

$$\begin{bmatrix} u_{mh} \\ u_{nh} \end{bmatrix} = R_s \begin{bmatrix} i_{mh} \\ i_{nh} \end{bmatrix} + \boldsymbol{L}_m \begin{bmatrix} \mathrm{p}i_{mh} \\ \mathrm{p}i_{nh} \end{bmatrix} + \omega_m \boldsymbol{L}_m \begin{bmatrix} -i_{nh} \\ i_{mh} \end{bmatrix} \tag{10}$$

where $\boldsymbol{L}_m$ is the inductance matrix in the mn-axes, and $\omega_m \boldsymbol{L}_m [i_{nh}, i_{mh}]^T$ is the rotational factor, which is induced by the coordinate transformation.

According to the spatial equivalent impedance model in Fig. 2, the mn-frame is a coupled coordinate system. Therefore, when the HF voltage is injected into the m-axis, the HF current responses are generated in both the m-axis and the n-axis. Besides, the voltage drop on R_s can be ignored. On this basis, the differential equations of PMSM can be written as follows:

$$\begin{cases} (L_{nn}/L_d L_q)\, U_m \sin(\omega_h t + \varphi_u) = di_{mh}/dt - \omega_m i_{nh} \\ (-L_{mn}/L_d L_q)\, U_m \sin(\omega_h t + \varphi_u) = di_{nh}/dt + \omega_m i_{mh} \end{cases}. \tag{11}$$

Then, i_{mh} can be expressed as follows:

$$i_{mh} = -A_p L_{nn} \cos(\omega_h t + \varphi_u) + B_p L_{mn} \sin(\omega_h t + \varphi_u) \tag{12}$$

where A_p and B_p can be written as follows:

$$A_p = \frac{U_{mh}\omega_h}{L_d L_q (\omega_h^2 - \omega_m^2)}, \quad B_p = \frac{U_{mh}\omega_m}{L_d L_q (\omega_h^2 - \omega_m^2)}. \tag{13}$$

According to (12), i_{mh} is a function relevant to θ_e. Therefore, θ_e can be obtained by calculating i_{mh}. Furthermore, the amplitudes of the HF current responses I_{mh} can be expressed as follows:

$$I_{mh} = \frac{U_{mh}\omega_h}{\omega_h^2 - \omega_m^2} \left(\frac{\cos^2\Delta\theta \sin\varphi_{du-i}}{L_d} + \frac{\sin^2\Delta\theta \sin\varphi_{qu-i}}{L_q} \right) \tag{14}$$

where $\Delta\theta = \theta_e - \theta_m$. $\varphi_{du\text{-}I}$ and $\varphi_{qu\text{-}I}$ are the phase differences between HF voltages and currents in the dq-axes.

However, in some high-resistance motors, the resistance will cause the distortion in I_{mh}. When considering R_s, i_{mh} can be rewritten as follows:

$$\begin{aligned} i_{mh} = {} & \frac{U_{mh}}{\omega_h L_d} \cos^2(\theta_m - \theta_e) \arcsin \frac{\omega_h L_d}{\sqrt{R_s^2 + \omega_h^2 L_d^2}} \sin(\omega_h t + \varphi_{idh}) \\ & + \frac{U_{mh}}{\omega_h L_q} \sin^2(\theta_m - \theta_e) \arcsin \frac{\omega_h L_q}{\sqrt{R_s^2 + \omega_h^2 L_q^2}} \sin(\omega_h t + \varphi_{iqh}) \end{aligned} \tag{15}$$

where φ_{idh} and φ_{iqh} is the phases of the HF currents. The phase difference can be expressed as follows:

$$\varphi_{di-qi} = \arcsin \frac{\omega_h L_d}{\sqrt{R_s^2 + \omega_h^2 L_d^2}} - \arcsin \frac{\omega_h L_q}{\sqrt{R_s^2 + \omega_h^2 L_q^2}}. \tag{16}$$

To verify the influence of the resistance effect on the fundamental component of the current curve, the FFT results of I_{mh} with different $\varphi_{di\text{-}qi}$ are shown in Fig. 5. Take $\theta_e = 30°$, $\varphi_{di\text{-}qi} = 40°$, and $\omega_m = 1$ rad/s as an example. The resistance effect introduces even-time harmonics of ω_m in L_{meq}^{-1}. However, the phase of fundamental frequency (2 Hz) is the same as the phase of $\varphi_{di\text{-}qi} = 0°$ (when $R_s = 0$). If the proposed method only extracts the fundamental components to estimate the initial

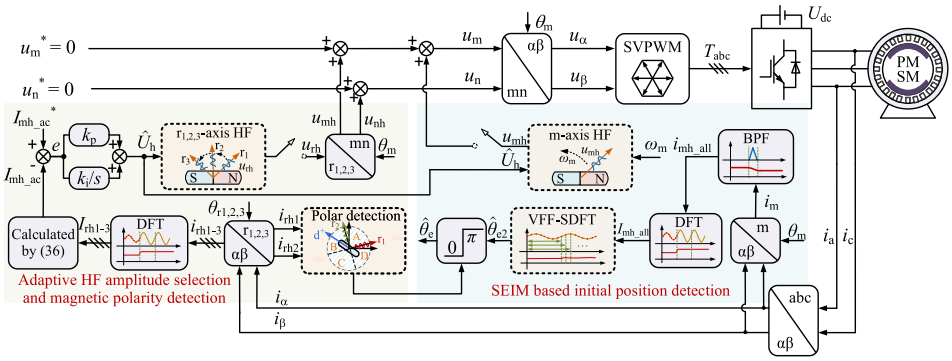

Fig. 4. Diagram of the proposed SEIM based rotor initial position detection method with HF injection.

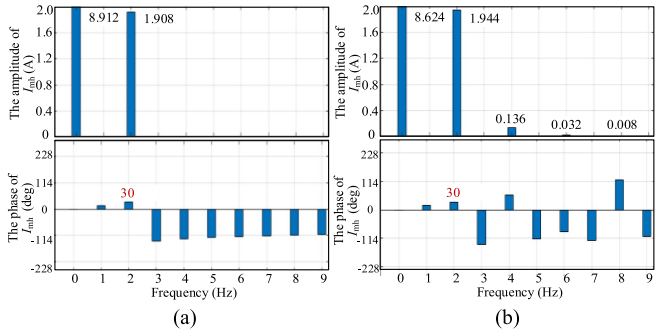

Fig. 5. FFT results of I_{mh} with different $\varphi_{\mathrm{di\text{-}qi}}$. (a) $\varphi_{\mathrm{di\text{-}qi}} = 0°$. (b) $\varphi_{\mathrm{di\text{-}qi}} = 40°$.

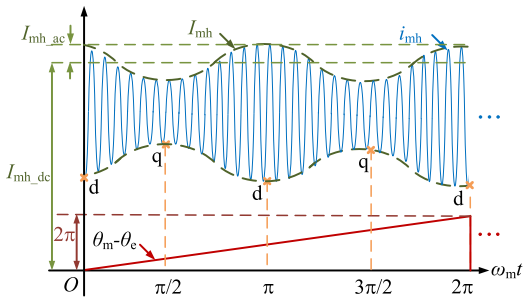

Fig. 6. Waveform of the HF current i_{mh} and the rotor position θ_{e}.

position, the resistance effect will not influence the estimated results.

Besides, the inverter nonlinearity effects can be viewed as an equivalent resistance in the *dq*-axes [31], the total resistance can be regarded as the series of the equivalent resistances and the stator resistance. Therefore, the inverter nonlinearity effects can also be neglected similarly.

Furthermore, considering the influence of cogging harmonics introduced by the cogging effect, the current response $I_{\mathrm{mh\_all}}$ can be written as follows:

$$\begin{aligned} I_{\mathrm{mh\_all}} &= U_{\mathrm{mh}}\omega_{\mathrm{h}} {L_{\mathrm{meq\_all}}}^{-1} / \left({\omega_{\mathrm{h}}}^2 - {\omega_{\mathrm{m}}}^2\right) \\ &= I_{\mathrm{mh}} + I_{\mathrm{mh\_har}} \cos\left(k_{\mathrm{h}}\omega_{\mathrm{m}} t + \varphi_{\mathrm{ac2}}\right) \\ &= I_{\mathrm{mh\_dc}} + I_{\mathrm{mh\_ac}} \cos\left(2\omega_{\mathrm{m}} t - 2\theta_{\mathrm{e}}\right) \\ &\quad + I_{\mathrm{mh\_har}} \cos\left(k_{\mathrm{h}}\omega_{\mathrm{m}} t + \varphi_{\mathrm{ac2}}\right) \end{aligned} \tag{17}$$

where $I_{\mathrm{mh\_har}}$ is a constant, and the current amplitude $I_{\mathrm{mh\_dc}}$ and $I_{\mathrm{mh\_ac}}$ can be expressed as follows:

$$\begin{cases} I_{\mathrm{mh\_dc}} = U_{\mathrm{mh}} L_{\Sigma}\omega_{\mathrm{h}} / L_{\mathrm{d}} L_{\mathrm{q}} \left({\omega_{\mathrm{h}}}^2 - {\omega_{\mathrm{m}}}^2\right) \\ I_{\mathrm{mh\_ac}} = U_{\mathrm{mh}} L_{\Delta}\omega_{\mathrm{h}} / L_{\mathrm{d}} L_{\mathrm{q}} \left({\omega_{\mathrm{h}}}^2 - {\omega_{\mathrm{m}}}^2\right) \end{cases}. \tag{18}$$

Therefore, the current response $I_{\mathrm{mh\_all}}$ consists of three components: a dc component, a fundamental component related to the rotor position, and a k_{h}/2th harmonic component. The dc component and the fundamental component correspond to the equivalent inductance ${L_{\mathrm{meq}}}^{-1}$, while the k_{h}/2-th harmonic component corresponds to ${L_{\mathrm{meq\_har}}}^{-1}$. Since the fundamental component contains the information of the rotor position, θ_{e} can be estimated by extracting the amplitude and phase of the fundamental component of $I_{\mathrm{mh\_all}}$.

Furthermore, according to (17), the waveforms of i_{mh}, I_{mh}, and θ_{m} are shown in Fig. 6. When the *m*-axis completes one rotational cycle at a speed of ω_{m}, I_{mh} can be expressed as a sinusoidal signal with $2\omega_{\mathrm{m}}$ frequency superimposed on a dc component. Let φ_{mh} denote the phase of I_{mh}. The estimated rotor position can be expressed as follows:

$$\hat{\theta}_{\mathrm{e}} = \left(\pi/2 - \varphi_{\mathrm{mh}}\right)/2. \tag{19}$$

$I_{\mathrm{mh\_all}}$ can be calculated by the DFT algorithm, which can be written as follows:

$$I_{\mathrm{mh\_all}}(\gamma) = \sqrt{\mathrm{Im}[D(\gamma)]^2 + \mathrm{Re}[D(\gamma)]^2} \tag{20}$$

where $D(i)$ represents the DFT sequence of the γth HF current cycle, and Im[] and Re[] represent the operations of calculating the imaginary and real parts, respectively. After calculating I_{mh}, θ_{e} can be estimated by (19) and φ_{mh} can be obtained by the VFF-SDFT algorithm presented in the next section.

B. VFF-SDFT Based Phase Calculation Algorithm

The DFT method can calculate the phase of the specified frequency signal. The DFT method is to transform the time-domain signal $I_{\mathrm{mh\_all}}$ mixed with different frequencies into frequency-domain signals, and calculate the amplitude and phase of the fundamental component of $I_{\mathrm{mh\_all}}$, respectively.

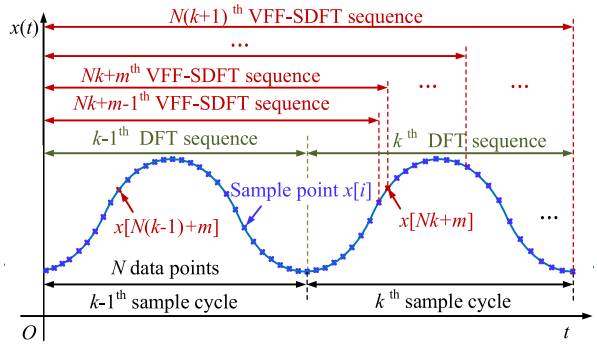

Fig. 7. Diagram of DFT sequence and the proposed VFF-SDFT sequence.

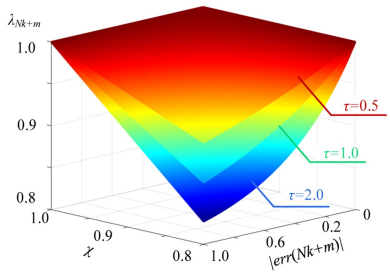

Fig. 8. Diagram of the relationship of the forgetting factor λ_{nk+m}, χ, and err.

I_{mh} is a low-frequency signal with a frequency of $2\omega_{\mathrm{m}}$. Therefore, the phase of I_{mh} can be calculated by the DFT method. However, the application of the traditional DFT algorithm for the phase calculation of I_{mh} will result in a slower update rate and lower data utilization efficiency during the rotor position calculation process. To address these limitations, this study proposes a VFF-SDFT algorithm for calculating the phase of I_{mh}. The proposed algorithm can improve the estimation speed and reduce the fluctuations of the estimation results.

The data sequence of the proposed VFF-SDFT algorithm is shown in Fig. 7. Within the computational windows of one DFT period, the VFF-SDFT algorithm demonstrates N calculation periods, significantly exceeding the operational frequency of the conventional DFT algorithm. Define the input signal as $x(i)$. N is the number of sample points. Since N is large, the SDFT has a high accuracy, which is beneficial when the SNR of the input signal is low. Therefore, $x(Nk+m)$ is the mth point of the kth period for VFF-SDFT, where k and m are subject to the following relationships:

$$\begin{cases} 0 \le m \le N-1 & m \in N \\ k \ge 0 & k \in N \end{cases}. \tag{21}$$

To ensure that the HF component and the low-frequency component can be accurately acquired, it is necessary to satisfy

$$N >> 2\pi f_{\mathrm{pwm}}/\omega_{\mathrm{h}}. \tag{22}$$

The SDFT sequence at the $Nk+m$ point can be expressed as follows:

$$\mathrm{SD}\,(Nk+m-1) = X^T E\,(Nk+m-1) + \mathrm{err}\,(Nk+m-1) \tag{23}$$

where $\boldsymbol{X}$ is the input signal matrix, $\boldsymbol{E}$ is the exponential factor matrix, and err is the disturbance signal vector.

Besides, the proposed VFF-SDFT sequence satisfies the following recursive relationship:

$$\begin{aligned}\mathrm{SD}\,(Nk+m) = {} & \mathrm{SD}\,(Nk+m-1) + \mathrm{SDIV}\,(Nk+m) \\ & -\mathrm{SDIV}\,(N\,(k-1)+m) + err\,(Nk+m)\end{aligned} \tag{24}$$

where SDIV is the iteration factor vector, which can be expressed as follows:

$$\begin{aligned}\mathrm{SDIV}\,(Nk+m) = {} & \lambda_{Nk+m}\mathrm{SDIV}\,(N\,(k-1)+m) \\ & +(1-\lambda_{Nk+m})\,x\,(Nk+m)\,e^{-j2\pi m/N}\end{aligned} \tag{25}$$

where λ is the forgotten factor in (0, 1). The initial value of the forgotten factor is

$$\mathrm{SDIV}\,(m) = x\,(m)\,e^{-j2\pi m/N}. \tag{26}$$

In (25), λ can be calculated by

$$\lambda_{Nk+m} = \chi + (1-\chi)\,e^{-\tau\|\mathrm{err}(Nk+m)\|} \tag{27}$$

where $0 < \chi < 1$, $\tau > 0$.

The forgetting factor λ_{nk+m} is related to the parameters χ, *err*, and τ, as shown in Fig. 8. When χ is constant, the larger the error vector *err* is, the smaller the forgetting factor λ_{nk+m} is. This means that the SDFT algorithm accounts for less weight at the old sampling points and more weight at the current sampling point, which indicates that the estimated initial position might be in the transient state. When the error vector err is close to zero, λ_{nk+m} is close to one, which indicates that the current point will not influence the estimated results significantly. Therefore, the system is in a steady state. When the error vector err is large, it indicates that the current point will influence the estimated results obviously, so the weight of the old data should be reduced. The parameter τ indicates the sensitivity to the disturbance error vector err. Parameter χ affects the range of the forgetting factor. The variable forgetting factor is in (χ, 1.0). χ is generally in (0.8, 0.98). The smaller the χ is, the faster the estimation speed is, but the poorer the steady-state performance is. The maximum of the forgetting factor is limited to 0.99 to ensure the utilization rate of the new data, which can ensure the stability under noise or transient states.

In the applications, χ should be selected first. When adjusting χ, set the parameter τ to infinity. λ_{nk+m} is approximately equal to the parameter χ. χ affects the minimum speed of the system. By adjusting χ, the acceptable speed range is determined. When adjusting τ, it is necessary to observe λ_{nk+m}. If λ_{nk+m} always goes down to χ in the steady state, it means that τ is too large. If λ_{nk+m} remains a large value in the transient state, it means that τ is too small.

In (27), the amplitude $A_{\rm err}$ and phase $\varphi_{\rm err}$ of err can be constructed by

$$\begin{cases} \varphi_{\rm err}\left(Nk+m\right) = \frac{1}{(k-1)N+m}\sum\limits_{i=N}^{Nk+m}\varphi\left(i\right) - \varphi\left(Nk+m\right) \\ A_{\rm err}\left(Nk+m\right) = \frac{1}{(k-1)N+m}\sum\limits_{i=N}^{Nk+m}A\left(i\right) - A\left(Nk+m\right) \end{cases} \tag{28}$$

where $A(i)$ and $\varphi(i)$ are the amplitude and phase of the sequence of the input signal, which can be calculated by the method in paper [32]. After that, $\varphi_{\rm mh}$ can be calculated and the initial position $\theta_{\rm e}$ can be estimated by (19).

C. Split-Step Injection Based Adaptive HF Amplitude Selection Method

In the initial position detection process, the HF current amplitude is determined by the HF voltage. A large response current will induce obvious noise. Conversely, a small current will lead to low accuracy. The proposed SSHI method selects the HF amplitude for different types of motors. Due to the low SNR of the motor with the low saliency ratio, different injection voltage amplitudes will significantly affect the initial position estimation accuracy. Therefore, the proposed SSHI method is meaningful to improve the estimation accuracy on PMSM with the low saliency ratio.

According to (17), $I_{\rm mh\_ac}$ decides the estimation precision of the initial position. To achieve a high SNR, $I_{\rm mh\_ac}$ must be at least ten times higher than the current sampling standard deviation $\sigma_{\rm err}$ in the experiment. And, the HF current value must be below the rated current I_N.

As shown in Fig. 5, $I_{\rm mh}$ reaches its maximum value when the m-axis becomes coincident with the d-axis, which can be expressed as follows:

$$I_{\rm m\_max} = \frac{U_{\rm m}\omega_{\rm h}}{\left({\omega_{\rm h}}^2 - {\omega_{\rm m}}^2\right)L_{\rm d}} \le I_N \tag{29}$$

where I_N is the rated current. Combining with (18), the relationship between HF current amplitude $I_{\rm mh\_ac}$ and $I_{\rm m\_max}$ can be expressed as follows:

$$I_{\rm mh\_ac} = I_{\rm m\_max}\left(1 - 1/\rho\right) \tag{30}$$

where ρ is the salience ratio. Besides, $I_{\rm mh}$ reaches its minimum value when the m-axis becomes coincident with the q-axis, which can be expressed as follows:

$$I_{\rm mh\_ac} = \left(\rho - 1\right)I_{\rm m\_min}. \tag{31}$$

Therefore, to achieve a high SNR, $I_{\rm mh\_ac}$ should meet

$$I_{\rm mh\_ac} \in \left[\max\left\{10\sigma_{\rm err},\ 10\left(\rho-1\right)\sigma_{\rm err}\right\},\ I_N\left(1-1/\rho\right)\right]. \tag{32}$$

According to (32), the minimum value of $I_{\rm mh\_ac}$ is chosen to be $10\sigma_{\rm err}$ when the ρ is small (less than 2). Conversely, the minimum value of $I_{\rm mh\_ac}$ is chosen to be $10(\rho–1)\,\sigma_{\rm err}$ when ρ is large (more than 2). ${I_{\rm mh\_ac}}^*$ is mainly determined by the saliency ratio and current sampling standard deviation. For IPMSM with $\rho > 2$, the current sampling standard deviation and the saliency ratio are the main determinants of ${I_{\rm mh\_ac}}^*$. According to (18) and (36), ρ can be obtained by $I_{\rm mh\_ac}$ and $I_{\rm mh\_dc}$, which can be expressed as follows:

$$\rho = \frac{1 + I_{\rm mh\_ac}/I_{\rm mh\_dc}}{1 - I_{\rm mh\_ac}/I_{\rm mh\_dc}}. \tag{33}$$

Therefore, the saliency ratio can be estimated online by the signals of the first cycle injected into the $r_{1,23}$-axes.

Besides, $I_{\rm mh\_ac}$ is relevant to $U_{\rm mh}$, which can be expressed as follows:

$$U_{\rm mh} = \frac{I_{\rm mh\_ac}L_{\rm d}L_{\rm q}\left({\omega_{\rm h}}^2 - {\omega_{\rm m}}^2\right)}{\omega_{\rm h}\left(L_{\rm q} - L_{\rm d}\right)} = \frac{I_{\rm mh\_ac}\left({\omega_{\rm h}}^2 - {\omega_{\rm m}}^2\right)}{X_{\rm m}\omega_{\rm h}} \tag{34}$$

where $X_{\rm m} = (L_{\rm d} - L_{\rm q})/L_{\rm d}L_{\rm q}$, represents the saliency of PMSMs.

When $I_{\rm mh\_ac}$ is obtained according to (32), the injected HF voltage can be calculated from (34). The relationship between $X_{\rm m}$ and $L_{\rm d,q}$ is shown in Fig. 9, where $X_{\rm m}$ is determined by $L_{\rm d}$ and $L_{\rm q}$. When ρ is smaller, $X_{\rm m}$ is smaller. When $L_{\rm d} = L_{\rm q}$, $X_{\rm m}$ is zero. In addition, the injected voltage $U_{\rm mh}$ is proportional to ${X_{\rm m}}^{-1}$. Therefore, the adaptive selection of $I_{\rm mh\_ac}$ can be realized by adjusting $U_{\rm mh}$.

In order to realize the adaptive selection of HF signal amplitude, the $r_1r_2r_3$ frame is established and the position relationship is shown in Fig. 10. The r_2- and r_3-axes are 90° and 45° ahead of the r_1-axis, respectively. The r_1-, r_2-, and r_3-axes are injected with HF voltage signals with an amplitude of $U_{\rm rh}$ and a frequency of $\omega_{\rm h}$, respectively. After that, the HF current of the r_1-, r_2-, and r_3-axes can be expressed as follows:

$$I_{{\rm rh}i} = \frac{U_{\rm rh}}{2\omega_{\rm h}}\left[\frac{1}{L_{\rm d}} + \frac{1}{L_{\rm q}} + \left(\frac{1}{L_{\rm d}} - \frac{1}{L_{\rm q}}\right)\cos(2\theta_{{\rm r}i} - 2\theta_{\rm e})\right] \quad i = 1, 2, 3. \tag{35}$$

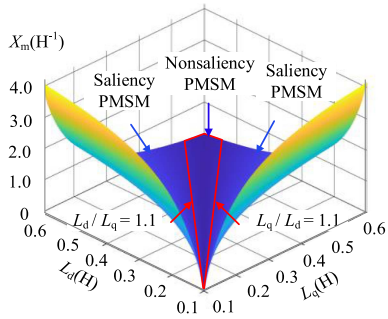

Fig. 9. Diagram of the relationship between $X_{\rm m}$ and $L_{\rm d,\ q}$.

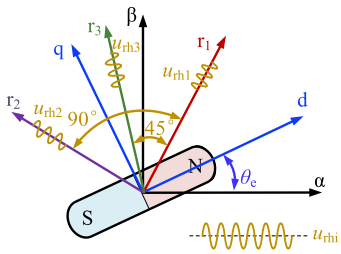

Fig. 10. Reference frames of PMSM for the adaptive HF amplitude selection.

After injecting HF voltages in the $r_1r_2r_3$-axes, $I_{\mathrm{mh\_dc}}$ and $I_{\mathrm{mh\_ac}}$ can be expressed as follows:

$$\begin{cases} I_{\mathrm{mh\_dc}} = (I_{\mathrm{rh1}} + I_{\mathrm{rh2}})/2 \\ I_{\mathrm{mh\_ac}} = \sqrt{(I_{\mathrm{rh1}} - I_{\mathrm{mh\_dc}})^2 + (I_{\mathrm{rh3}} - I_{\mathrm{mh\_dc}})^2} \end{cases}. \tag{36}$$

Then, $I_{\mathrm{mh\_ac}}$ differs from the given value $I_{\mathrm{mh\_ac}}{}^*$. Afterward, the HF voltage amplitude is obtained by the PI regulator until the error converges to zero, which can be expressed as follows:

$$\hat{U}_{\mathrm{mh}} = k_{\mathrm{ph}} \cdot (I_{\mathrm{mh\_ac}}{}^* - I_{\mathrm{mh\_ac}}) + k_{\mathrm{ih}} \int (I_{\mathrm{mh\_ac}}{}^* - I_{\mathrm{mh\_ac}})\,\mathrm{d}t. \tag{37}$$

To make the initial response value around 0.5 times the given value, set $k_{\mathrm{ph}} = L_\Delta/L_{\mathrm{d}}L_{\mathrm{q}}\omega_{\mathrm{h}}$ according to (34). k_{ih} is decided by the update period T_{si}. $k_{\mathrm{ih}} < 0.5k_{\mathrm{ph}}/T_{\mathrm{si}}$ is selected in the proposed SSHI method to ensure stability.

The block diagram of the adaptive HF signal amplitude selection method is shown in Fig. 4. A given value $I_{\mathrm{mh\_ac}}{}^*$ is achieved by adjusting the value of U_{mh} online. At the same time, the magnetic polarity detection can be realized by the HF current peak-value accumulation method.

D. Magnetic Polarity Detection

Conventional double-pulse injection methods will cause high noise and potential damage to permanent magnets. In order to avoid the problems, the magnetic polarity detection method based on peak accumulation is proposed, which is carried out in the process of adaptive HF signal amplitude selection. The proposed method achieves magnetic polarity detection by accumulating the peak value of positive and negative currents in the r_1- and r_2-axes. The following principles should meet.

Principle 1: When the injection signal has a component in the positive d-axis, the saturation degree of the d-axis increases, resulting in L_{d} decreasing.

Principle 2: One of the following should meet.

1) When the HF current components in the q-axis are positive, the saturation degree of the q-axis increases ($i_{\mathrm{q}} > 0$ before injection), which leads to $L_{\mathrm{q}}{}^+ < L_{\mathrm{q}}{}^-$, and $I_{\mathrm{qx}}{}^+ > I_{\mathrm{qx}}{}^-$.
2) When the HF current components in the q-axis are positive, the saturation degree of the q-axis decreases ($i_{\mathrm{q}} < 0$ before injection), which leads to $L_{\mathrm{q}}{}^+ > L_{\mathrm{q}}{}^-$, and $I_{\mathrm{qx}}{}^+ < I_{\mathrm{qx}}{}^-$.
3) The saturation degree of the q-axis does not change due to the symmetry ($i_{\mathrm{q}} = 0$ before injection), so $I_{\mathrm{qx}}{}^+ = I_{\mathrm{qx}}{}^-$.

When the HF voltage signals are injected into the r_1- and r_2-axes, the HF voltage u_{dx} and u_{qx} can be expressed as follows:

$$\begin{bmatrix} u_{\mathrm{d}x} \\ u_{\mathrm{q}x} \end{bmatrix} = \begin{bmatrix} U_m \sin(\omega_h t + \varphi_x)\cos(\theta_{\mathrm{r}x}) \\ U_m \sin(\omega_h t + \varphi_x)\sin(\theta_{\mathrm{r}x}) \end{bmatrix} \mathrm{x} = 1,\ 2 \tag{38}$$

where φ_x is the phase of $u_{\mathrm{d}x}$ and $u_{\mathrm{q}x}$.

Take $i_{\mathrm{q}} = 0$ as an example. Define $I_{\mathrm{d,q}x}{}^+$ and $I_{\mathrm{d,q}x}{}^-$ as the positive and negative maximums of HF current in the dq-axes. According to the principle of nonlinear magnetization of the iron core, if $L_{\mathrm{d}}{}^+ < L_{\mathrm{d}}{}^-$, then $I_{\mathrm{d}x}{}^+ > I_{\mathrm{d}x}{}^-$. Besides, the saturation of the q-axis is less affected by the injection signal, $L_{\mathrm{q}}{}^+ = L_{\mathrm{q}}{}^-$, so $I_{\mathrm{q}x}{}^+ = I_{\mathrm{q}x}{}^-$. Considering the relationship between the dq-axes current response, there is $I_{\mathrm{r}x}{}^+ > I_{\mathrm{r}x}{}^-$. Therefore, by comparing $I_{\mathrm{r}x}{}^+$ and $I_{\mathrm{r}x}{}^-$, the rotor position can be divided into four regions

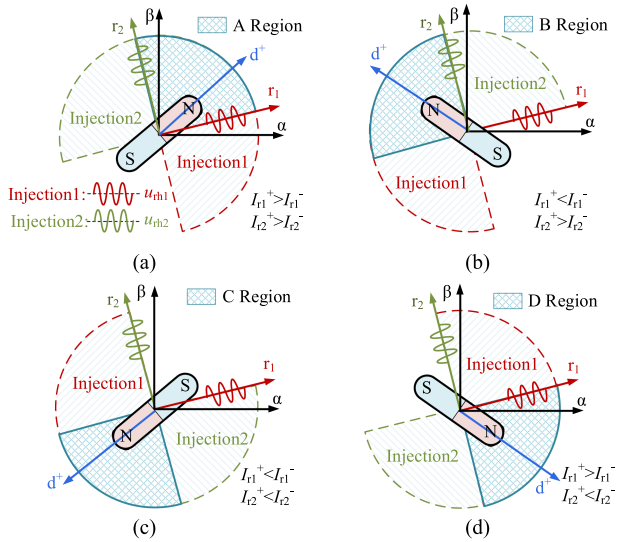

Fig. 11. Diagram of $I_{\mathrm{r}x}{}^+$ and $I_{\mathrm{r}x}{}^-$ with different N-pole positions. (a) A Region. (b) B Region. (c) C Region. (d) D Region.

TABLE I
RESULTS AND JUDGMENT CONDITIONS

Conditions	Region
$N_{\mathrm{c1}} > \eta N_{\mathrm{all}}$	A or D
$N_{\mathrm{c2}} > \eta N_{\mathrm{all}}$	C or D
$N_{\mathrm{c1}} < (1-\eta) N_{\mathrm{all}}$	B or C
$N_{\mathrm{c2}} < (1-\eta) N_{\mathrm{all}}$	A or B

A, B, C, and D. As shown in Fig. 11, the N-pole position is in region A when $I_{\mathrm{r1}}{}^+ > I_{\mathrm{r1}}{}^-$ and $I_{\mathrm{r2}}{}^+ > I_{\mathrm{r2}}{}^-$, in region B when $I_{\mathrm{r1}}{}^+ < I_{\mathrm{r1}}{}^-$and $I_{\mathrm{r2}}{}^+ > I_{\mathrm{r2}}{}^-$, in region C when $I_{\mathrm{r1}}{}^+ < I_{\mathrm{r1}}{}^-$ and $I_{\mathrm{r2}}{}^+ < I_{\mathrm{r2}}{}^-$, and in region D when $I_{\mathrm{r1}}{}^+ > I_{\mathrm{r1}}{}^-$ and $I_{\mathrm{r2}}{}^+ < I_{\mathrm{r2}}{}^-$. Similar to $i_{\mathrm{q}} = 0$ before injection, when $i_{\mathrm{q}} \neq 0$, there must be an r_x-axis, leading to the significant differences of the peak values. The region of the magnetic pole can be detected by comparing the current peaks with significant differences.

A comprehensive comparison of all samples should be carried out when comparing $I_{\mathrm{r}x}{}^+$ and $I_{\mathrm{r}x}{}^-$. So, a threshold η is set to avoid polarity misjudgment. Let the number of sample points satisfying $I_{\mathrm{r1}}{}^+ > I_{\mathrm{r1}}{}^-$, $I_{\mathrm{r2}}{}^+ > I_{\mathrm{r2}}{}^-$ be N_{c1} and N_{c2}, respectively. The total number of samples is N_{all}. According to the current relationship shown in Fig. 10, the judgment conditions in Table I can be derived, where η takes its value in (0, 1). After detecting the magnetic polarity region, the final rotor position can be obtained by the SEIM method.

When the obtained region contains the rotor position, the magnetic polar compensation is not required. On the contrary, compensation is required. Therefore, the magnetic polarity can be obtained by only the r_1 or r_2-axis. However, it might cause misjudgments when the axis is close to the q-axis. Under this condition, the magnetic polar region can be detected by the r_x-axis, which is close to the estimated position or the difference is about 180°. So, the double injections in the r_1- and r_2-axes are necessary since the angle difference is 90°.

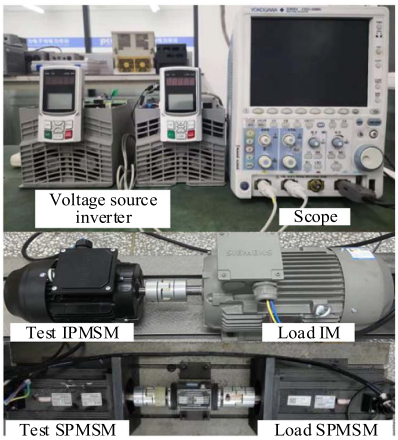

Fig. 12. Experimental platforms of 2.2 kW IPMSM and 7.5 kW SPMSM drives.

TABLE II
IPMSM PARAMETERS

Parameter	Value	Parameter	Value
Rated Power	2.2 kW	Resistance	2.5 Ω
Rated Speed	1500 r/min	d-axis inductance	22.0 mH
Rated Frequency	75 Hz	q-axis inductance	52.0 mH
Rated Current	4.4 A	Flux linkage	0.53 Wb
Rated Torque	14 N·m	Number of Pole Pairs	3

TABLE III
SPMSM PARAMETERS

Parameter	Value	Parameter	Value
Rated Power	7.5 kW	Resistance	0.27 Ω
Rated Speed	1500 r/min	d-axis inductance	1.05 mH
Rated Frequency	100 Hz	q-axis inductance	1.05 mH
Rated Current	20.0 A	Flux linkage	0.4 Wb
Rated Torque	48 N·m	Number of Pole Pairs	4

IV. EXPERIMENTAL RESULTS

The proposed method is validated on a 2.2 kW IPMSM and a 7.5 kW SPMSM experimental platform shown in Fig. 12 with the parameters in Tables II and III. The dc bus voltage is 537 V. The experimental platform is based on the STM32F103 microcontroller. The carrier frequency of the IPMSM is 6 kHz, and the carrier frequency of the SPMSM is 8 kHz.

In the experiment, ω_{h} is chosen to be 500 Hz for reducing the resistance effect. The estimation time can be adjusted by ω_{m}. When ω_{m} is higher, N is lower, which will cause the SDFT method to be more sensitive to noise and lead to the accuracy loss. The lower ω_{m} is, the higher the accuracy is, but the longer the time is. In this article, considering the influence of accuracy and time, ω_{m} is chosen to be 10 Hz. The experimental result of the initial position detection is shown in Fig. 13, where the rotor position is 43.2°. The estimation results of the rotor position calculated by DFT, SDFT, and VFF-SDFT are 44.93°, 44.30°, and 44.21°, respectively. The fluctuations of results with VFF-SDFT are 0.96°.

In addition, the experiment results with different ω_{m} are shown in Fig. 14. When the m-axis rotational frequency is 5 Hz, the initial position estimation time is 110 ms with the fluctuation

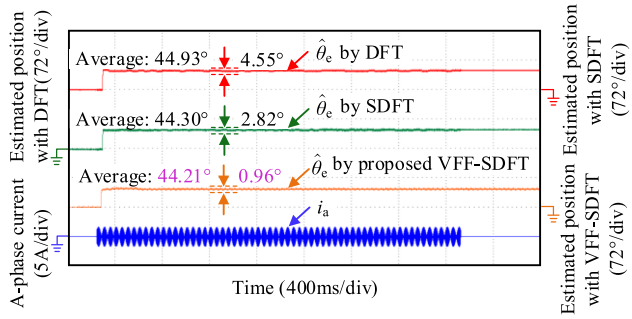

Fig. 13. Experimental results for DFT, SDFT, and VFF-SDFT with $\theta_{\mathrm{e}} = 43.2°$.

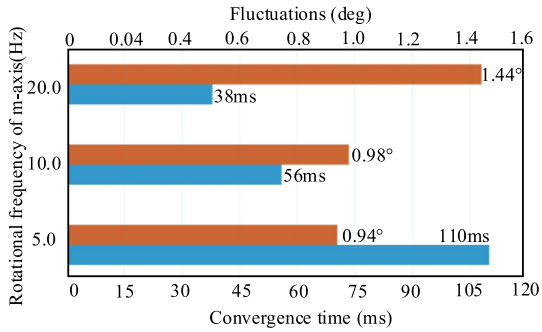

Fig. 14. Experimental results with different rotational speeds of the m-axis.

of 0.94°. When the frequency is 10 Hz, the time is 56 ms with the fluctuation of 0.98°. When the frequency is 20 Hz, the time is 38 ms with the fluctuation of 1.44°. Considering that 56 ms can satisfy most application scenarios, 10 Hz is chosen as the m-axis rotational frequency.

The experimental waveforms of the adaptive HF signal amplitude selection and magnetic polarity detection process are shown in Fig. 15, where $I_{\mathrm{mh\_ac}}{}^{*}$ is 0.62 A and the positions of r_1, r_2, and r_3 are 0°, 90°, and 45°, respectively. ρ is estimated to be about 2.2 by the HF injection, which is close to the rated value. The HF signal amplitude is stabilized within five injection cycles. At the same time, the magnetic polarity is obtained from the HF current response $I_{\mathrm{r1,2}}$. The waveforms of N_{c1}, N_{c2}, and N_{all} are shown in Fig. 15(b), where η is 0.7. When θ_{e} is 0°, N_{c1} and N_{c2} are accumulated to 258 and 153, respectively, which account for 86% and 51% of N_{all}, respectively. Therefore, the rotor magnetic pole is in the A or D region. Similarly, when θ_{e} is 45°, N_{c1} and N_{c2} are accumulated to 249 and 240, respectively. The rotor magnetic pole is in the A region.

The overall experimental waveform of the rotor initial position detection is shown in Fig. 16. χ is 0.85 and τ is 0.12 for IPMSM, while χ is 0.85 and τ is 0.08 for SPMSM. In the first 1.0 s, the HF signal amplitude adaptive selection and magnetic polar region detection are executed, after which the initial position detection is applied. Fig. 16(a) shows the experimental results of the IPMSM, where $I_{\mathrm{mh\_ac}}{}^{*}$ is given as 0.62 A. The SSHI method takes about 335 ms, while the SEIM based method takes about 59 ms. The estimation result is 72.47° and the real value is 72.00°, thus, the error is –0.47°. Fig. 16(b) shows the experimental results of SPMSM. $I_{\mathrm{mh\_ac}}{}^{*}$ is given as 0.4 A. The

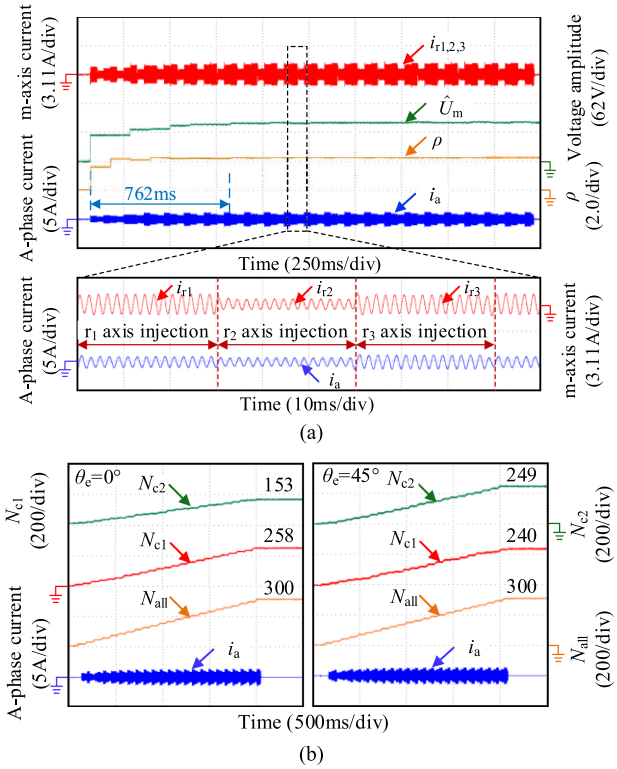

Fig. 15. Experimental waveforms in the process of the HF amplitude selection and magnetic polarity detection. (a) HF amplitude selection. (b) Magnetic polarity detection.

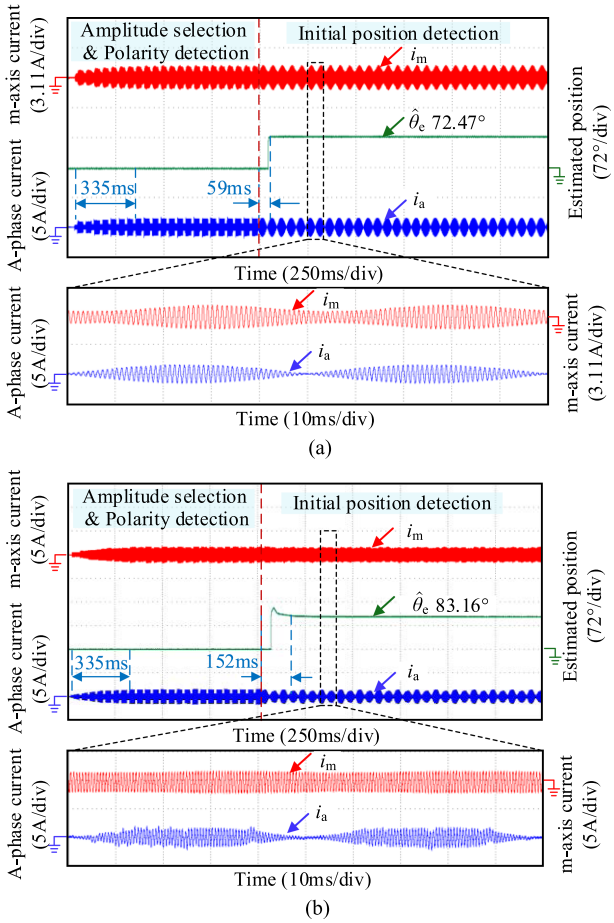

Fig. 16. Experimental waveforms of the initial position detection. (a) On the IPMSM with $\theta_e = 72.00°$. (b) On the SPMSM with $\theta_e = 81.60°$.

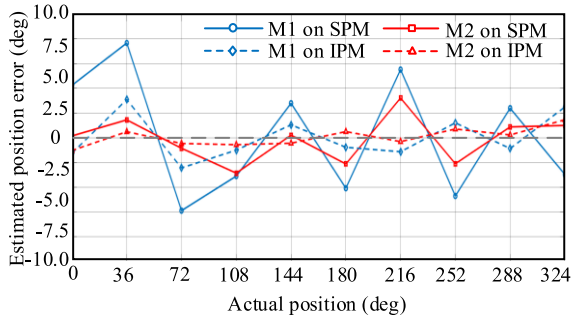

Fig. 17. Experimental results with different θ_e on SPMSM and IPMSM.

SSHI method takes about 335 ms, while the SEIM based method takes about 152 ms. The real value is 81.60° and the estimation result is 83.16° with an error of –1.56°.

Fig. 17 shows the experimental results of initial position detection with different electrical angles, where M1 represents the rotary injection method proposed in paper [12] and M2 represents the proposed SEIM based method. It can be seen that the initial position detection errors of the SEIM method are within 1.45° for IPMSM and 3.20° for the SPMSM. The proposed method achieves a higher estimation accuracy.

The method is verified on motors with different saliency ratios by injecting *d*-axis dc currents. When the experimental saliency ratios are 1.10, 1.05, and 1.028, the experimental waveforms are shown in Fig. 18. Fig. 18(a) shows the experimental results of the initial position estimation with a saliency ratio of 1.10, whose convergence time is 98 ms and the error is –1.18° with the fluctuation of 0.97°. Fig. 18(b) shows the results when the saliency ratio is 1.05, whose convergence time is 103 ms and the error is 3.35° with the fluctuation of 2.46°. Fig. 18(c) shows the experimental results with a saliency ratio of 1.028, whose convergence time is 115ms and the error is 5.49° with the fluctuation of 7.34°. The lowest saliency ratio is 1.028 when the proposed method maintains effectiveness.

Fig. 19 shows the experimental waveforms of the proposed method and the conventional method on IPMSM. Fig. 19(a) shows the estimation result of M1 method. When θ_e is 216°, the estimation result of the conventional method is 217.14° with an error of –1.14° and the fluctuation is 2.41°. Fig. 19(b) shows the experimental results of the proposed method. When θ_e is 216°, the estimation result of the proposed method is 216.32° with an error of –0.32°, and the fluctuation is 0.75°. On IPMSM, the proposed SEIM method takes about 70 ms, while the method in [12] takes about 40 ms. The convergence time of the proposed method is close to the conventional method. Besides, the double-pulse injection process has been left out.

Fig. 20 shows the experimental waveforms of the proposed method and the conventional method on SPMSM. When θ_e is 61.2°, the estimation result of the conventional method is 52.18° with an error of 9.02° and the fluctuation of the estimation result

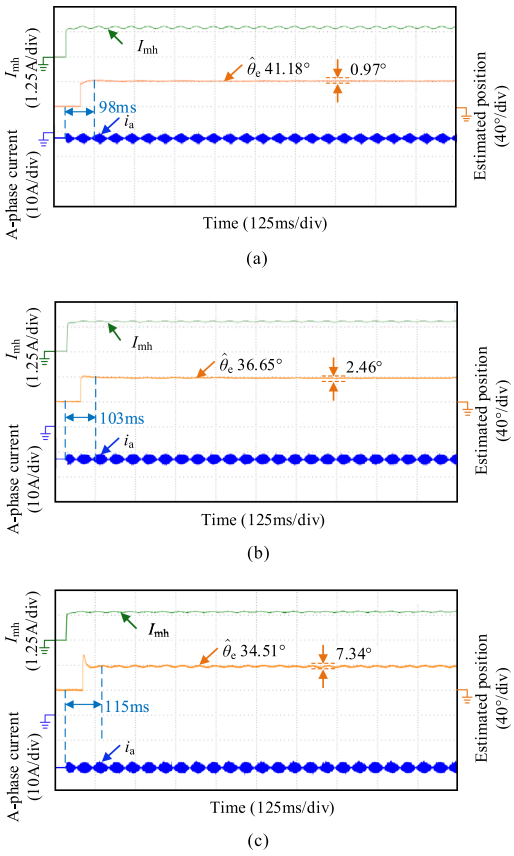

Fig. 18. Experimental results for the SEIM method with different saliency ratios when $\theta_e = 40°$. (a) $\rho = 1.10$. (b) $\rho = 1.05$. (c) $\rho = 1.028$.

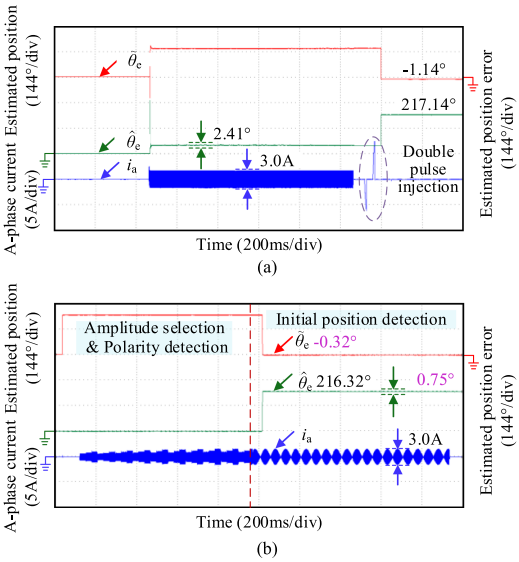

Fig. 19. Experimental results of the SEIM method and conventional method with $\theta_e = 216°$ on IPMSM. (a) Conventional method. (b) SEIM method.

is 2.23°. The estimation result of the proposed method is 60.45° with an error of 0.75° and the fluctuation is 0.98°. On SPMSM, the proposed SEIM method takes about 220 ms, while the method in [12] takes about 50 ms. But the estimation precision is improved significantly. In addition, the stator current amplitude of the proposed method is 2.9 A, while the conventional method

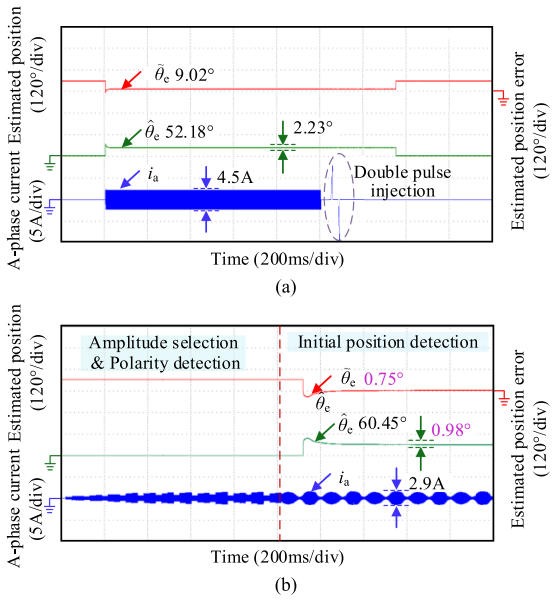

Fig. 20. Experimental results of the SEIM method and conventional method with $\theta_e = 61.2°$ on SPMSM. (a) Conventional method. (b) SEIM method.

is 4.5 A. The current amplitude of the proposed method is smaller.

V. Conclusion

In this article, an HF signal injection initial position detection method based on the SEIM has been proposed. The proposed method takes the position estimation errors caused by the motor cogging harmonics into account and has a higher estimation accuracy. In addition, an adaptive HF voltage amplitude selection method based on split-step HF injection is proposed to improve the estimation accuracy of different PMSMs. Simultaneously, magnetic polarity detection is applied. The effectiveness and universality of the proposed method have been verified by experiments. During the initial position detection process, the injection amplitude is smaller, and the estimation precision is higher. Additionally, the double-pulse injection process is replaced to avoid damage to the permanent magnets. Therefore, this method provides an effective solution for the initial position detection of PMSMs with significant cogging harmonics introduced by cogging effects. The initial position detection accuracy will be improved significantly, particularly for SPMSMs with the low saliency.

References

[1] J. Lee, Y.-C. Kwon, and S.-K. Sul, "Signal-injection sensorless control with tilted current reference for heavily saturated IPMSMs," *IEEE Trans. Ind. Electron.*, vol. 35, no. 11, pp. 12100–12109, Nov. 2020.

[2] K. Wang, G. Wang, G. Zhang, Q. Wang, B. Li, and D. Xu, "ESO-based robust hybrid flux observer with active flux error estimation for position sensorless PMa-SynRM drives," *IEEE Trans. Transp. Electrific.*, vol. 11, no. 1, pp. 2049–2060, Feb. 2025.

[3] G. Zhang et al., "Adaptive step-size predictive PLL based rotor position estimation method for sensorless IPMSM drives," *IEEE Trans. Power Electron.*, vol. 39, no. 5, pp. 6136–6147, May 2024.

[4] X. Fu, Y. Xu, H. He, and X. Fu, "Initial rotor position estimation by detecting vibration of permanent magnet synchronous machine," *IEEE Trans. Ind. Electron.*, vol. 68, no. 8, pp. 6595–6606, Aug. 2021.
[5] L. Shen, J. Wu, and S. Yang, "Initial position estimation in SRM using bootstrap circuit without predefined inductance parameters," *IEEE Trans. Power Electron.*, vol. 26, no. 9, pp. 2449–2456, Sep. 2011.
[6] H. Wang, J. Wang, and W. Xu, "A high precision initial position estimation method for low saliency ratio machine based on image tracking," *IEEE Trans. Power Electron.*, vol. 38, no. 11, pp. 13612–13624, Nov. 2023.
[7] Z. Wang, Z. Cao, and Z. He, "Improved fast method of initial rotor position estimation for interior permanent magnet synchronous motor by symmetric pulse voltage injection," *IEEE Access*, vol. 8, pp. 59998–60007, 2020.
[8] K. Lin, P. Wang, P. Cai, X. Wu, and M. Lin, "Fast initial rotor position estimation for IPMSM with unipolar sequence-pulse injection," *IEEE Trans. Energy Convers.*, vol. 36, no. 4, pp. 3545–3554, Dec. 2021.
[9] H. Pairo, B. Nikmaram, and S. Mohamadian, "Adaptive-based accurate rotor initial position estimation in synchronous reluctance motors," *IEEE Trans. Ind. Electron.*, vol. 71, no. 11, pp. 13812–13821, Nov. 2024.
[10] Z. Zhu, A. Almarhoon, and P. Xu, "Improved rotor position estimation accuracy by rotating carrier signal injection utilizing zero-sequence carrier voltage for dual three-phase PMSM," *IEEE Trans. Ind. Electron.*, vol. 64, no. 6, pp. 4454–4462, Jun. 2017.
[11] P. Chen, R. Ma, H. Bai, Z. Chen, and S. Song, "Rotating high frequency voltage injection strategy considering time delay for PMSM based on dual heterodyne method," *IEEE Trans. Energy Convers.*, vol. 40, no. 2, pp. 901–910, Jun. 2025.
[12] X. Jin, R. Ni, W. Chen, F. Blaabjerg, and D. Xu, "High-frequency voltage-injection methods and observer design for initial position detection of permanent magnet synchronous machines," *IEEE Trans. Power Electron.*, vol. 33, no. 9, pp. 7971–7979, Sep. 2018.
[13] G. Wang, M. Valla, and J. Solsona, "Position sensorless permanent magnet synchronous machine drives—A review," *IEEE Trans. Ind. Electron.*, vol. 67, no. 7, pp. 5830–5842, Jul. 2020.
[14] G. Wang, D. Xiao, G. Zhang, C. Li, X. Zhang, and D. Xu, "Sensorless control scheme of IPMSMs using HF orthogonal square-wave voltage injection into a stationary reference frame," *IEEE Trans. Power Electron.*, vol. 34, no. 3, pp. 2573–2584, Mar. 2019.
[15] G. Bi, G. Wang, G. Zhang, N. Zhao, and D. Xu, "Low-noise initial position detection method for sensorless permanent magnet synchronous motor drives," *IEEE Trans. Power Electron.*, vol. 35, no. 12, pp. 13333–13344, Dec. 2020.
[16] S. Dong, M. Zhou, X. You, and C. Wang, "A sensorless control strategy of injecting HF voltage into d-axis for IPMSM in full speed range," *IEEE Trans. Power Electron.*, vol. 37, no. 11, pp. 13587–13597, Nov. 2022.
[17] M. A. Ghazi Moghadam and F. Tahami, "Sensorless control of PMSMs with tolerance for delays and stator resistance uncertainties," *IEEE Trans. Power Electron.*, vol. 28, no. 3, pp. 1391–1399, Mar. 2013.
[18] C. Li, G. Wang, G. Zhang, D. Xu, and D. Xiao, "Saliency-based sensorless control for SynRM drives with suppression of position estimation error," *IEEE Trans. Ind. Electron.*, vol. 66, no. 8, pp. 5839–5849, Aug. 2019.
[19] S. Liu et al., "Virtual-axis injection based online parameter identification of PMSM considering cross coupling and saturation effects," *IEEE Trans. Power Electron.*, vol. 38, no. 5, pp. 5791–5802, May 2023.
[20] Q. Tang, A. Shen, X. Luo, and J. Xu, "IPMSM sensorless control by injecting bidirectional rotating HF carrier signals," *IEEE Trans. Power Electron.*, vol. 33, no. 12, pp. 10698–10707, Dec. 2018.
[21] G. Bi, G. Zhang, G. Wang, Q. Wang, Y. Hu, and D. Xu, "Adaptive iterative learning control-based rotor position harmonic error suppression method for Sensorless PMSM drives," *IEEE Trans. Ind. Electron.*, vol. 69, no. 11, pp. 10870–10881, Nov. 2022.
[22] Q. Wang et al., "Zero-sequence voltage error elimination-based offline VSI nonlinearity identification for PMSM drives," *IEEE Trans. Transp. Electrific.*, vol. 10, no. 1, pp. 55–66, Mar. 2024.
[23] S. Wang, J. Hong, Y. Sun, and H. Cao, "Analysis of zeroth-mode slot frequency vibration of integer slot permanent-magnet synchronous motors," *IEEE Trans. Ind. Electron.*, vol. 67, no. 4, pp. 2954–2964, Apr. 2020.
[24] S. Ray and D. Dey, "Development of a comprehensive analytical model of induction motor under stator interturn faults incorporating rotor slot harmonics," *IEEE Trans. Ind. Electron.*, vol. 70, no. 2, pp. 2037–2047, Feb. 2023.
[25] B. Wen, K. Liu, Z.-Q. Zhu, and R. Ding, "Estimation of magnet temperature for integer-slot permanent magnet synchronous machines via extraction of first-order slot harmonic in back EMF," *IEEE Trans. Transp. Electrific.*, vol. 10, no. 3, pp. 7203–7213, Sep. 2024.
[26] I. Szalay, D. Fodor, K. Enisz, and H. Medve, "Saliency model extension for sensorless initial position and polarity detection of permanent magnet synchronous motors," *IEEE Access*, vol. 9, pp. 168292–168314, 2021.
[27] X. Wu, Z. Zhu, and Z. Wu, "A rotor initial position estimation method for surface-mounted permanent magnet synchronous machine," *IEEE Trans. Energy Convers.*, vol. 36, no. 3, pp. 2012–2024, Sep. 2021.
[28] Z. Q. Zhu and L. M. Gong, "Investigation of effectiveness of sensorless operation in carrier-signal-injection-based sensorless-control methods," *IEEE Trans. Ind. Electron.*, vol. 58, no. 8, pp. 3431–3439, Aug. 2011.
[29] M. Tanaskovic, C. Zhao, F. Percacci, P. Gnos, S. Mariethoz, and D. Frick, "Rotor polarity detection and tracking for slotless permanent magnet synchronous motors," in *Proc. IEEE 9th Int. Symp. Sensorless Control Elect. Drives*, 2018, pp. 102–107.
[30] Y. S. Jeong, R. D. Lorenz, T. M. Jahns, and S. K. Sul, "Initial rotor position estimation of an interior permanent-magnet synchronous machine using carrier-frequency injection methods," *IEEE Trans. Ind. Appl.*, vol. 41, no. 1, pp. 38–45, Jan./Feb. 2005.
[31] Q. Wang, G. Zhang, G. Wang, C. Li, and D. Xu, "Offline parameter self-learning method for general-purpose PMSM drives with estimation error compensation," *IEEE Trans. Power Electron.*, vol. 34, no. 11, pp. 11103–11115, Nov. 2019.
[32] Q. Wang, G. Wang, N. Zhao, G. Zhang, Q. Cui, and D. Xu, "An impedance model-based multiparameter identification method of PMSM for both offline and online conditions," *IEEE Trans. Power Electron.*, vol. 36, no. 1, pp. 727–738, Jan. 2021.

Qiyao Li received the B.S. degree in electrical engineering from the Harbin Institute of Technology, Harbin, China, in 2023. He is currently working toward the Ph.D. degree in power electronics and electrical drives in the Harbin Institute of Technology, Harbin, China.

His current research interests include permanent magnet synchronous motors (PMSMs) parameter identification technique, and PMSM initial position detection technique.

Qiwei Wang (Member, IEEE) received the B.S., M.S., and Ph.D. degrees from the Harbin Institute of Technology, Harbin, China, in 2015, 2017, and 2022, respectively, all in electrical engineering.

He is currently an Associate Professor in power electronics and electrical drives with the School of Electrical Engineering and Automation, Harbin Institute of Technology. His current research interests include parameter identification technique and permanent magnet synchronous motor position sensorless control.

Gaolin Wang (Senior Member, IEEE) received the B.S., M.S., and Ph.D. degrees from the Harbin Institute of Technology, Harbin, China, in 2002, 2004, and 2008, respectively, all in electrical engineering.

In 2009, he joined the Department of Electrical Engineering, Harbin Institute of Technology, as a Lecturer, where he has been a Full Professor of electrical engineering since 2014. From 2009 to 2012, he was a Postdoctoral Fellow with Shanghai Step Electric Corporation. He has authored more than 70 technical papers published in IEEE Transactions. He is the holder of 40 Chinese patents. His current major research interests include permanent magnet synchronous motor drives and power converters.

Dr. Wang serves as a Guest Associate Editor of IEEE TRANSACTIONS ON INDUSTRIAL ELECTRONICS, an Associate Editor of IEEE TRANSACTIONS ON TRANSPORTATION ELECTRIFICATION, and *IET Electric Power Applications*.

Fengxiang Wang (Senior Member, IEEE) was born in Jiujiang, China, in 1982. He received the B.S. degree in electronic engineering and the M.S. degree in automation from Nanchang Hangkong University, Nanchang, China, in 2005 and 2008, respectively, and the Ph.D. degree in electrical engineering from the Institute for Electrical Drive Systems and Power Electronics, Technical University of Munich, Munich, Germany, in 2014.

He is currently a Full Professor and Deputy Director with the Quanzhou Institute of Equipment Manufacturing, Haixi Institutes, Chinese Academy of Sciences, Jinjiang, China. His research interests include predictive control and sensorless control for electrical drives and power electronics.

Dr. Wang is an Associate Editor for IEEE TRANSACTIONS ON INDUSTRIAL ELECTRONICS and IEEE TRANSACTIONS ON ENERGY CONVERSION. As a General Chair, he organized IEEE 5th International Symposium on Predictive Control of Electrical Drives and Power Electronics. He is a Fellow of the Institution of Engineering and Technology.

Guoqiang Zhang (Senior Member, IEEE) received the B.S. degree from Harbin Engineering University, Harbin, China, in 2011, and the M.S. and Ph.D. degrees from the Harbin Institute of Technology, Harbin, in 2013 and 2017, respectively, all in electrical engineering.

Since then, he has been a Postdoctoral Fellow and a Lecturer with the Department of Electrical Engineering, Harbin Institute of Technology. His current research interests include parameter identification technique, and control of electrical drives, with main focus on sensorless field-oriented control of interior permanent magnet synchronous machines.

Dr. Zhang serves as an Associate Editor for *Journal of Power Electronics*.

Dianguo Xu (Fellow, IEEE) received the B.S. degree in control engineering from Harbin Engineering University, Harbin, China, in 1982, and the M.S. and Ph.D. degrees in electrical engineering from the Harbin Institute of Technology (HIT), Harbin, in 1984 and 1989, respectively.

In 1984, he was an Assistant Professor with the Department of Electrical Engineering, HIT. Since 1994, he has been a Professor with the Department of Electrical Engineering, HIT. He was the Dean of School of Electrical Engineering and Automation, HIT, from 2000 to 2010. He was the Vice President of HIT, from 2014 to 2020. He has authored or coauthored more than 600 technical papers. His research interests include motor drives, PMSM servo drives, renewable energy generation technology, and power quality mitigation.

Dr. Xu serves as the Co-EIC for IEEE TRANSACTIONS ON POWER ELECTRONICS, and an Associate Editor for IEEE TRANSACTIONS ON INDUSTRIAL ELECTRONICS and IEEE JOURNAL OF EMERGING AND SELECTED TOPICS IN POWER ELECTRONICS. He is currently the Chairperson of IEEE Harbin Section.